T2R2 東京科学大学 リサーチリポジトリ
Science Tokyo Research Repository

論文 / 著書情報
Article / Book Information

Title	Effects of metal, oxide, and hybrid metal-oxide interlayers on spin–orbit torque in BiSb topological insulator and magnetic interfaces
Authors	Quang Le, Xiaoyong Liu, Lei Xu, Brian R. York, Cherngye Hwang, Son Le, Maki Maeda, Tuo Fan, Yu Tao, Hisashi Takano, Min Liu, Zhang Ruixian, Shota Namba, Pham Nam Hai
Citation	Journal of Applied Physics, Vol. 137, , pp. 123903
Pub. date	2025, 3
Note	This article may be downloaded for personal use only. Any other use requires prior permission of the author and AIP Publishing. This article appeared in Journal of Applied Physics, Vol. 137, , pp. 123903 and may be found at https://doi.org/10.1063/5.0253596.

Powered by T2R2 (Science Tokyo Research Repository)

Journal of Applied Physics

RESEARCH ARTICLE | MARCH 25 2025

Effects of metal, oxide, and hybrid metal-oxide interlayers on spin–orbit torque in BiSb topological insulator and magnetic interfaces

Quang Le ; Xiaoyong Liu ; Lei Xu ; Brian R. York; Cherngye Hwang ; Son Le ; Maki Maeda ; Tuo Fan ; Yu Tao ; Hisashi Takano; Min Liu ; Zhang Ruixian; Shota Namba; Pham Nam Hai

Check for updates

J. Appl. Phys. 137, 123903 (2025)
https://doi.org/10.1063/5.0253596

View Online
Export Citation

Articles You May Be Interested In

High temperature spin Hall effect in topological insulator

Appl. Phys. Lett. (June 2023)

High spin Hall angle in BiSb topological insulator and perpendicularly magnetized CoFeB/MgO multilayers with metallic interfacial layers

Appl. Phys. Lett. (February 2024)

Low power spin–orbit torque switching in sputtered BiSb topological insulator/perpendicularly magnetized CoPt/MgO multilayers on oxidized Si substrate

Appl. Phys. Lett. (August 2021)

26 March 2025 01:42:43

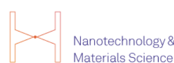

Unlock the Full Spectrum.
From DC to 8.5 GHz.
Your Application. Measured.
Find out more
Zurich Instruments

AIP Publishing

Journal of Applied Physics | ARTICLE | pubs.aip.org/aip/jap

Effects of metal, oxide, and hybrid metal-oxide interlayers on spin–orbit torque in BiSb topological insulator and magnetic interfaces

Cite as: J. Appl. Phys. **137**, 123903 (2025); doi: 10.1063/5.0253596
Submitted: 18 December 2024 · Accepted: 7 March 2025 ·
Published Online: 25 March 2025

Quang Le,[1,a)] Xiaoyong Liu,[1] Lei Xu,[1] Brian R. York,[2] Cherngye Hwang,[2] Son Le,[1] Maki Maeda,[3] Tuo Fan,[3] Yu Tao,[3] Hisashi Takano,[3] Min Liu,[2] Zhang Ruixian,[2] Shota Namba,[2] and Pham Nam Hai[2,a)]

AFFILIATIONS

[1]Western Digital Corp., Great Oaks site, San Jose, California 95119, USA
[2]Department of Electrical and Electronic Engineering, Institute of Science Tokyo, Tokyo 152-8552, Japan
[3]Western Digital Corp., Fujisawa site, Kanagawa 252-0811, Japan

[a)]**Authors to whom correspondence should be addressed:** quang.le@wdc.com and pham.n.ab@m.titech.ac.jp

ABSTRACT

The charge-to-spin conversion efficiency at the interface between a topological insulator and a ferromagnetic (FM) layer can be enhanced by inserting an interlayer (ITL). However, the mechanism of this enhancement is unclear. In this work, we systematically investigate the ITL effects by introducing various metal, oxide, and hybrid metal/oxide ITL between a BiSb topological insulator and a CoFe ferromagnetic layer. Our findings revealed that using a metallic NiFeGe or insulating MgO ITL resulted in similarly high efficiencies, with the highest efficiency achieved when employing hybrid NiFeGe/MgO ITL. However, efficiency decreased when NiFeGe was combined with MgTiO with increasing TiO composition. Such behaviors can be qualitatively understood by considering the ITL intrinsic effect of enhancing the intrinsic spin Hall angle of BiSb via preventing Sb diffusion from BiSb and migration of the FM and the extrinsic effect where the ITL spin transparency is determined by the spin tunneling/diffusion across the ITL and the spin-flip/spin-transfer at the ITL/FM interface. This study provides valuable insights and a framework for understanding and optimizing interlayer materials for ultralow power spin–orbit torque applications.

© 2025 Author(s). All article content, except where otherwise noted, is licensed under a Creative Commons Attribution-NonCommercial-NoDerivs 4.0 International (CC BY-NC-ND) license (https://creativecommons.org/licenses/by-nc-nd/4.0/). https://doi.org/10.1063/5.0253596

26 March 2025 01:42:43

I. INTRODUCTION

Efficient manipulation of magnetization through spin currents in nonvolatile magnetic memory devices, such as magnetoresistive random-access memory (MRAM), is essential for the low-power operation of neuromorphic computing systems utilizing them—particularly, in edge AI chips. Consequently, spin–orbit torque (SOT) has emerged as a leading mechanism, where charge currents induce spin currents and vice versa, in non-magnetic materials exhibiting strong spin–orbit coupling (SOC). The strength of SOC and its correlation with the spin Hall angle (θ_{SH}) is articulated in Eq. (1), where J_S denotes the spin current density and J_C represents the charge current density,

$$\theta_{SH} = \frac{J_S}{J_C}\frac{2e}{\hbar}. \tag{1}$$

The spin Hall angle θ_{SH} due to the intrinsic mechanism (i.e., Berry phase) can be, in principle, larger than unity.[1] Yet it is usually smaller than 1 in many well-studied heavy metals, such as Pt,[2] W,[3] or Ta.[4] The small θ_{SH} not only requires large driving transistors for SOT-MRAM, which makes it challenging to integrate with Si circuitry, but also limits the writing speed. To fully exploit the advantages of SOT-MRAM, we need to use materials with a giant $\theta_{SH} > 1$. Recently, several topological quantum materials with nontrivial band structures, such as Bi_2Se_3,[5] $(Bi,Sb)_2Te_3$,[6] and BiSb[7] topological insulators (TIs) and YPtBi topological semimetals (TSM),[8–10] have shown such a giant θ_{SH}. Among them, BiSb has attracted considerable attention as a promising SOT material candidate for future energy-efficient SOT device applications because it shows both giant room-temperature θ_{SH} and high electrical conductivity,[11] and industrial tools can deposit it.[12,13]

However, the research on this BiSb material is still in its early stages, and the related physical, material, and device optimization remains to be addressed. One significant issue is the relatively low thermal and chemical stability of BiSb, which can sometimes introduce atomic diffusion. Specifically, this involves the migration of Sb from BiSb to the adjacent ferromagnetic (FM) and buffer layers, as well as the movement of FM materials into the BiSb layer. Such diffusion results in a decreased charge-to-spin conversion efficiency for BiSb, ultimately hindering the SOT energy efficiency of BiSb/FM's film stack. To resolve this problem, we and other groups have demonstrated that inserting a non-magnetic (NM) metallic or oxide interlayer between BiSb (TI) and the ferromagnetic layer (FM) can enhance the charge-to-spin conversion efficiency at the BiSb–FM interfaces.[14–18] However, the underlying mechanism behind this enhancement is not well understood.

In this work, we aim to investigate and compare the effects of inserting metal, oxide, and hybrid metal-oxide interlayers such as NiFeGe, MgO, NiFeGe/MgO, and NiFeGe/MgTiO, respectively, in between the BiSb and FM layers. We not only observe how effectively they can enhance the charge-to-spin conversion efficiency but also study the mechanism behind their effects. For this study, we select the interlayer's materials, use transport and structural analyses to compare them, and rank them based on their effectiveness in blocking Sb diffusion, acting as a migration and shunt barrier, transferring crystal symmetry from BiSb to the ferromagnetic layer, and preventing the ferromagnetic dead layer to improve the spin transport across the BiSb/FM interface. First, to determine the interlayers' relative efficiency, we evaluate their damping-like SOT efficiency per unit current density, ξ^{j}_{DL}, or effective spin Hall angle θ^{eff}_{SH}, which is a function of the product of T_{IST}, the interfacial spin transparency, and θ_{SH}, the intrinsic spin Hall angle, as given by Eq. (2),[19]

$$\xi^{j}_{DL} \equiv \theta^{eff}_{SH} = T_{IST}\theta_{SH}. \tag{2}$$

Then, we will use a phenomenological model to explain the impact of each type of interlayer on ξ^{j}_{DL}. In particular, we will discuss the two different effects of the interlayer (ITL) on ξ^{j}_{DL}: an intrinsic effect related to θ_{SH} and an extrinsic effect related to T_{IST}. Our study can provide a useful framework for understanding ultra-high ξ^{j}_{DL} and guidance on increasing it by optimizing the TI's interlayer material for ultralow power SOT applications.

II. EXPERIMENT PROCEDURE

The whole BiSb stack consists of a buffer, a 10 nm BiSb layer, a matrix of interlayers by wafer, a ferromagnetic (FM) 0.7 nm $Co_{40}Fe_{60}$ layer, and a capping layer that was deposited at room temperature on a silicon oxide substrate after a conventional cleaning process, followed by a light sputter etch inside a physical vapor deposition tool. The buffer and matrix of the interlayers are designed to promote BiSb (012) orientation, prevent migration and Sb diffusion, and offer greater resistivity than BiSb to minimize shunting. A series of interlayer materials, including metals, oxides, and hybrid metal/oxides such as NiFeGe, MgO, NiFeGe/MgO, and NiFeGe/MgTiO were incorporated into the BiSb stacks for a comparative analysis of their effectiveness on ξ^{j}_{DL} and impact on θ_{SH} and T_{IST}. Structural, thickness, composition, and orientation characterization of the BiSb stacks with a matrix of interlayers were confirmed by using x-ray diffraction (XRD), x-ray reflectivity (XRR), and x-ray fluorescence (XRF), respectively. Transmission electron microscopy (TEM) was conducted on the BiSb stacks to confirm and validate XRR, XRF, and XRD data. Figure 1 shows a typical stack structure and cross section TEM.

A vibrating sample magnetometer (VSM) was utilized to extract the FM's saturation magnetization. We utilized Resistivity mapping probe (Resmap) measurements to understand the topological insulating nature of the BiSb stacks. In this work, ξ^{j}_{DL} is obtained by exploiting the second harmonics Hall technique. A prober equipped with a direct current (DC)/alternating current (AC) source, a lock-in amplifier, and a 1 T-capable electromagnet was used to measure both the anomalous Hall resistance and the second harmonic Hall signal in the BiSb stacks fabricated into Hall bars. An AC is applied in-plane to the BiSb/FM Hall bar, generating an alternating pure spin current due to the spin Hall effect. This spin current diffuses to the adjacent FM layer across the interface, subsequently exerting an SOT on the FM layer. Consequently, the FM's magnetization

26 March 2025 01:42:43

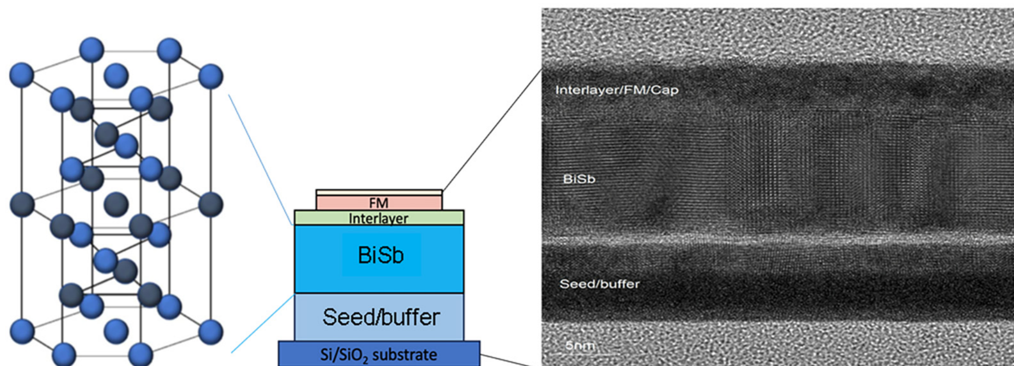

FIG. 1. The representative BiSb stack consists of seed/buffer layers, a 10 nm BiSb layer, a matrix of interlayers by wafer, an FM layer, and a capping layer deposited at room temperature.

© Author(s) 2025

oscillation as the result of the SOT gives rise to the second harmonic Hall voltage response, which is characterized by Eq. (3) for the case of in-plane magnetization,[20]

$$R_{\mathrm{H}}^{2\omega} = \frac{R_{\mathrm{AHE}}}{2}\left(\frac{H_{\mathrm{AD}}}{H_{\mathrm{k}} + H_{\mathrm{x}}}\right) + \alpha_{\mathrm{ONE}} H_{\mathrm{x}} + R_{\mathrm{ANE+SSE}}, \tag{3}$$

where $R_{\mathrm{H}}^{2\omega}$ is the second harmonic Hall resistance, R_{AHE} is the anomalous Hall resistance, H_{AD} is the anti-damping-like field, H_{k} is the effective magnetic anisotropy field, H_{x} is the in-plane applied magnetic field, α_{ONE} is the ordinary Nernst effect coefficient, and $R_{\mathrm{ANE+SSE}}$ is a constant representing contribution of the anomalous Nernst effect and spin Seebeck effect. In this analysis, we neglect the contributions from a field-like torque, which is known to be very small in BiSb based on earlier studies.[21] Figure 2(a) illustrates the measurement circuit using Hall bar devices. The fabricated Hall bar devices have four terminals and measure $10 \times 25\,\mu\mathrm{m}^2$. We first measured R_{AHE} and H_{k} with a DC bias and a perpendicular magnetic field. Then, we applied AC bias and used the lock-in amplifier to measure $R_{\mathrm{H}}^{2\omega}$ while sweeping an in-plane magnetic field along the x direction. We then fit the $R_{\mathrm{H}}^{2\omega} - H_{\mathrm{x}}$ data into Eq. (3) to estimate H_{AD} and plot H_{AD} as a function of the current density inside BiSb, J_{BiSb}. Finally, we estimate $\xi_{\mathrm{DL}}^{\mathrm{j}}$ from the slope of $\frac{H_{\mathrm{AD}}}{J_{\mathrm{BiSb}}}$ as shown in the following Eq. (4),

$$\xi_{\mathrm{DL}}^{\mathrm{j}} = (2e/\hbar) M_{\mathrm{S}} t_{\mathrm{FM}} \frac{H_{\mathrm{AD}}}{J_{\mathrm{BiSb}}}, \tag{4}$$

where M_{S} is the measured saturation magnetization of the FM layer and $t_{\mathrm{FM}} = 0.7$ nm is its thickness.

Figure 2(b) shows an example of the AHE measurement of a sample consisting of a buffer layer, a 10 nm-thick BiSb layer, a 1.2 nm MgO interlayer, a 0.7 nm-thick CoFe FM layer, and a capping layer, measured with a perpendicular magnetic field. The data show that $R_{\mathrm{AHE}} = 1.7\,\Omega$ and $H_{\mathrm{k}} = 6$ kOe for this sample, which were then used to fit the $R_{\mathrm{H}}^{2\omega} - H_{\mathrm{x}}$ data to Eq. (3). Figure 2(c) shows the $R_{\mathrm{H}}^{2\omega}$ measurement (points) and the corresponding fitting (solid lines) at different bias AC from 3.5 to 6.5 mA with a 1 mA step. Here, we scan H_{x} to get two sectors of $R_{\mathrm{H}}^{2\omega}$ data at each bias AC. Then, we plot the H_{AD} values obtained by fitting the sectors to Eq. (3) and plot them as a function of J_{BiSb} in Fig. 2(d). We also prepared a reference stack without the BiSb layer to determine each stack's BiSb conductivity and used

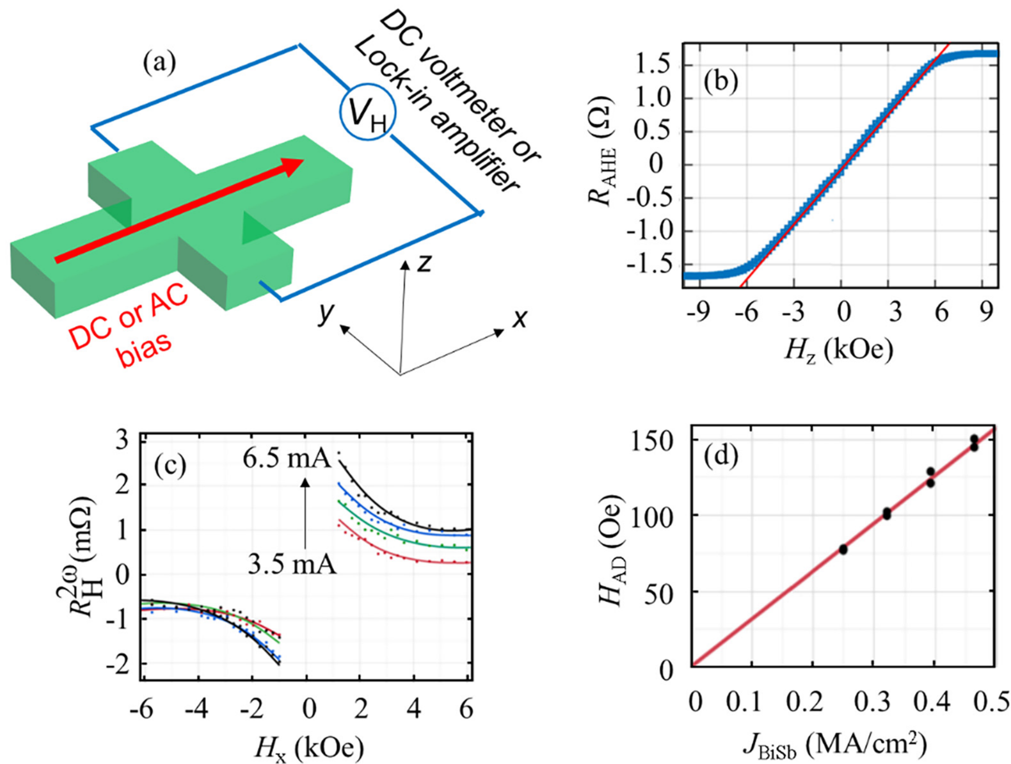

FIG. 2. Representative measurement of a sample with a 10 nm-thick BiSb layer, a 1.2 nm MgO interlayer, and a 0.7 nm-thick CoFe FM layer. (a) Illustration of the measurement circuit. (b) Anomalous Hall resistance measured with a perpendicular magnetic field. The solid line is used for estimation of $H_{\mathrm{k}} = 6$ kOe. (c) Second harmonic Hall resistance (points) and the corresponding fitting (solid lines) at different bias AC from 3.5 to 6.5 mA with a 1 mA step. (d) Damping-like field H_{AD} as a function of the current density J_{BiSb} in BiSb, estimated from (c). The straight line indicates the slope $H_{\mathrm{AD}}/J_{\mathrm{BiSb}}$.

26 March 2025 01:42:43

© Author(s) 2025

this information to calculate J_{BiSb}. Finally, from the H_{AD}/J_{BiSb} slope, we obtained $\xi_{DL}^{j} = 5.2$ in this stack.

III. PHENOMENOLOGICAL MODELING OF ξ_{DL}^{j} IN TI/INTERLAYER/FM SYSTEMS

Since BiSb is a TI with 2D topological surface states that dominate current-in-plane charge transport at the studied thickness (10 nm),[11,12] one can apply a model that incorporates the Edelstein effect (EE) in a TI-based system consisting of a TI/NM/FM or TI/IS/FM tri-layer system, as schematically shown in Fig. 3.[22–25]

Here, the NM or IS is collectively referred to as an interlayer. In this type of system, the surface states in a topological insulator (TI) are protected due to spin-momentum locking. Therefore, a direct relationship exists between a 2D charge density J_C^{2D} in TI and the spin potential at the TI interface. As such, tunneling/diffusion and spin-flip scattering processes in the adjacent layers can impact the final generated spin current J_S. A 2D charge-to-spin conversion efficiency q_{EE} is defined by $q_{EE} = J_S/J_C^{2D}$, which is equivalent to ξ_{DL}^{j} via $\xi_{DL}^{j} = (t_{BiSb}/2) \times q_{EE}$, where t_{BiSb} is the BiSb layer thickness. Consequently, q_{EE} with the tunneling/diffusion and spin-flip scattering processes involved in EE is given as[22–25]

$$q_{EE} = \frac{1}{V_F(\tau_t + \tau_{sf})}, \tag{5}$$

where V_F is the Fermi velocity, τ_t is the electron tunneling/diffusion time across the TI/ITL interface, and τ_{sf} is the spin-flip time that happens in the ITL and at the ITL/FM interface. When a charge current is applied to the TI layer at an optimal thickness for surface conductivity, it generates a spin potential on the TI/ITL interface. The spins must tunnel through and overcome the potential barrier at the TI/ITL interface, diffuse across the ITL, and finally overcome the potential barrier at the ITL/FM interface. During these processes, spin-flip scattering may happen in the ITL layer or at the ITL/FM interface. Since we keep the ITL thin (1.2 nm), we assume that the spin-flip/spin-transferring time τ_{mix} at the ITL/FM interface dominates and we replace τ_{sf} by τ_{mix} in Eq. (5). The physical meaning of τ_{mix} in the denominator of Eq. (5) is that the spin current requires a gradient of the spin potential across the ITL, which becomes steeper with shorter τ_{mix}, i.e., the faster the spin is flipped or transferred to the FM at the ITL/FM interface, the higher spin current can flow. As such, for a TI/ITL/FM system, the contribution of τ_t and τ_{mix} varies, where τ_t depends on the tunnel barrier height for the insulating oxide ITL, while τ_{mix} is determined by spin-mixing conductance $g_{mix}^{\uparrow\downarrow}$ at the ITL/FM interface $\tau_{mix} \sim \frac{1}{g_{mix}^{\uparrow\downarrow}}$.[22] Note that the equation assumes a perfect TI surface state with perfect spin-momentum locking. In reality, a finite spin potential will be generated depending on the details of the TI properties. Therefore, one should consider a finite intrinsic θ_{SH} as a prefactor before considering the q_{EE} effect. The final measured ξ_{DL}^{j} efficiency will be proportional to $(\tau_t + \tau_{mix})^{-1}\,\theta_{SH}$ for a constant TI thickness. In other words, T_{IST}, the interfacial spin transparency in Eq. (2), is proportional to $(\tau_t + \tau_{mix})^{-1}$.

Our phenomenological model assumes two different effects of the ITL on ξ_{DL}^{j}: An intrinsic effect related to θ_{SH} and an extrinsic effect related to $T_{IST} \propto (\tau_t + \tau_{mix})^{-1}$. These reflect the important intrinsic and extrinsic benefits of inserting ITL between the TI and the FM. First, the ITL materials play a crucial role in stabilizing the TI at the TI/ITL interface by preventing Sb diffusion away from BiSb and the migration of materials from the FM layer, which helps maintain a better spin-momentum locked surface state. Suppose the FM and TI layers are directly in contact. In that case, the hybridization of orbitals may change the topological surface band structure, and the magnetic interaction from the FM with a local magnetic moment may potentially destroy the surface TI state,[26,27] resulting in smaller intrinsic θ_{SH}. Second, there is a connection between T_{IST} with τ_t and τ_{mix} as discussed above. T_{IST} is more related to τ_{mix} if the ITL is a metal, but if the ITL is an insulator, T_{IST} is more related to τ_t. Furthermore, metallic ITL materials typically increase FM diffusion and create disorder at the ITL/FM interface,[28,29] which in turn lowers $g_{mix}^{\uparrow\downarrow}$ (longer τ_{mix}) at the ITL/FM

26 March 2025 01:42:43

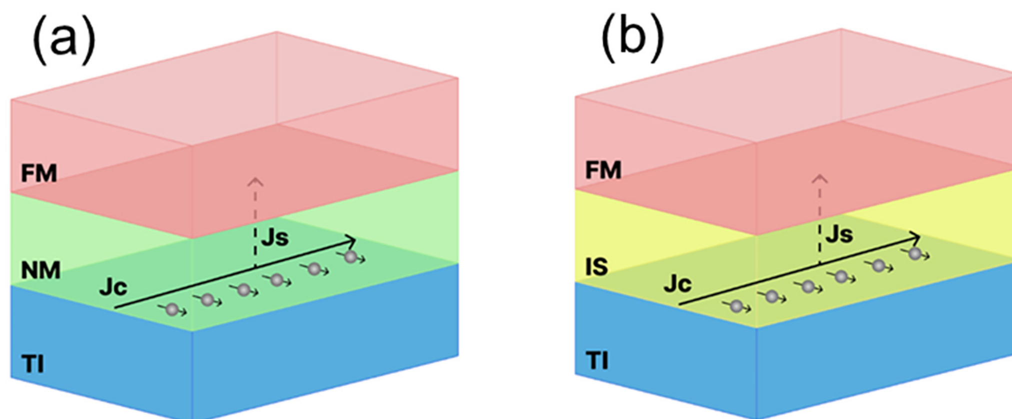

FIG. 3. Schematics for the spin Hall effect in a topological insulator with (a) a non-magnetic metal (NM) or (b) an insulating oxide (IS) interlayer sandwiched between BiSb (TI) and a ferromagnetic (FM) layer.

© Author(s) 2025

interface; however, they tend to have shorter τ_t. Conversely, insulating ITL materials can preserve the integrity of the FM, decreasing disorder at the ITL/FM interface. This reduction results in higher $g_{mix}^{\uparrow\downarrow}$ (shorter τ_{mix}) at the interface, although insulating materials are associated with longer tunneling τ_t. Therefore, the careful selection of ITL materials is needed to improve both θ_{SH} (intrinsic effect) and spin current transportation by minimizing both τ_t and τ_{mix} (extrinsic effect). This model can provide a useful framework for understanding ultrahigh ξ_{DL}^{j} and guidance on increasing it by optimizing the TI's interlayer material for potential SOT applications.

IV. ξ_{DL}^{j} OF METAL, OXIDE, AND HYBRID METAL-OXIDE INTERLAYERS

To validate this phenomenological model, a comparative study of metal, oxide, and hybrid metal-oxide interlayers was performed to determine their influence on ξ_{DL}^{j}. Prior to initiating the investigation, TEM and XRD were employed to confirm the BiSb baseline film stack for the BiSb (012) orientation. Figure 4 illustrates an example of the BiSb film stack, which features a NiFeGe/MgO ITL configuration for the purpose of illustration, serving as a baseline representation of the metal, oxide, and hybrid metal-oxide interlayers examined in this research. This stack is positioned between the BiSb (012) layer and a CoFe layer with magnetization in the film plane.

Notably, the XRD analysis depicted in Fig. 5 confirms that the appropriate buffer layer beneath the BiSb, which exhibits high-intensity counts, can enhance the BiSb (012) orientation.

Figure 6 shows ξ_{DL}^{j} of sample N with no ITL, sample A_1 with a NiFeGe (12 Å) ITL, sample A_2 with an MgO (12 Å) ITL, sample B with a hybrid NiFeGe (9 Å)/MgO (3 Å) ITL, and samples C_1–C_3 with a NiFeGe (9 Å)/$Mg_{1-x}Ti_xO$ (3 Å) ILT whose x was 0.33, 0.37, and 0.44, respectively. A closer examination of Fig. 6 reveals a large ξ_{DL}^{j} in the samples A_1 and A_2 with NiFeGe and MgO ITL, while the maximum ξ_{DL}^{j} is achieved in the sample B with the hybrid NiFeGe/MgO ITL, and it decreases in samples C_1–C_3 with the NiFeGe/MgTiO ITL whose TiO concentration gradually increases. In comparison, we only observed ξ_{DL}^{j} of 0.2 for the sample N without an ILT. This result clearly shows that selecting an optimal interlayer can effectively tune θ_{SH} and the spin transmission into the FM layer and hence ξ_{DL}^{j}.

To understand the experimental observation by using our proposed phenomenological model, we summarize the ITL, their intrinsic effect on θ_{SH}, their extrinsic effect on T_{IST} via τ_t and τ_{mix}, and the resulting effect on ξ_{DL}^{j} in Table I.

From the model's vantage point, the enhancement of ξ_{DL}^{j} in sample A_2 with a single MgO (12 Å) ITL may initially seem counterintuitive. Generally, introducing insulators in the ITL typically increases the potential barrier, so the tunneling time τ_t increases, ultimately reducing ξ_{DL}^{j}. Furthermore, thin MgO has been used to suppress spin pumping and reduce the magnetization damping factor of the free magnetic layer in STT-MRAM. In our case, however, inserting a MgO layer between the TI and FM can prevent unwanted interaction between the FM and TI, leading to an intrinsic effect with improved θ_{SH}. More specifically, the direct interaction between the FM and BiSb surface disrupts the BiSb surface state by altering the TI band structure, including changes to the Fermi level or potentially creating other surface states. Thus, the intrinsic benefit of the enhanced θ_{SH} overcomes the loss due to the extrinsic effect (longer τ_t), and the MgO interlayer helps increase ξ_{DL}^{j}.

26 March 2025 01:42:43

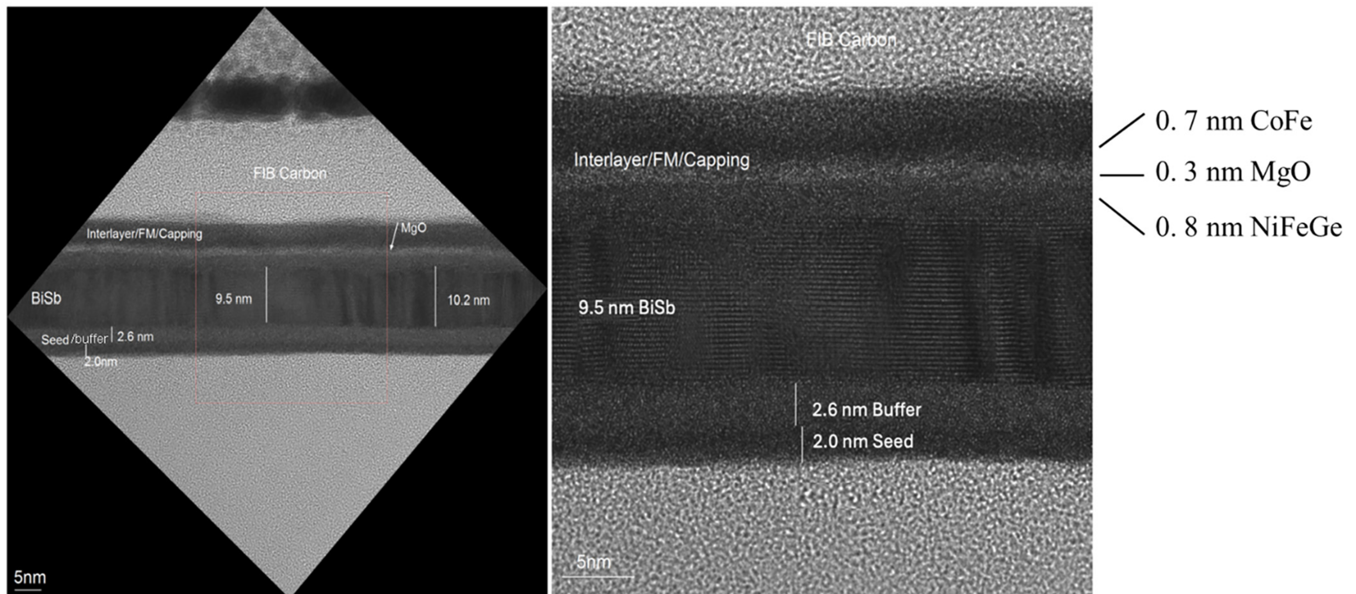

FIG. 4. The BiSb film stack, which features a NiFeGe/MgO configuration, is a baseline representation of the metal, oxide, and hybrid metal-oxide interlayers.

© Author(s) 2025

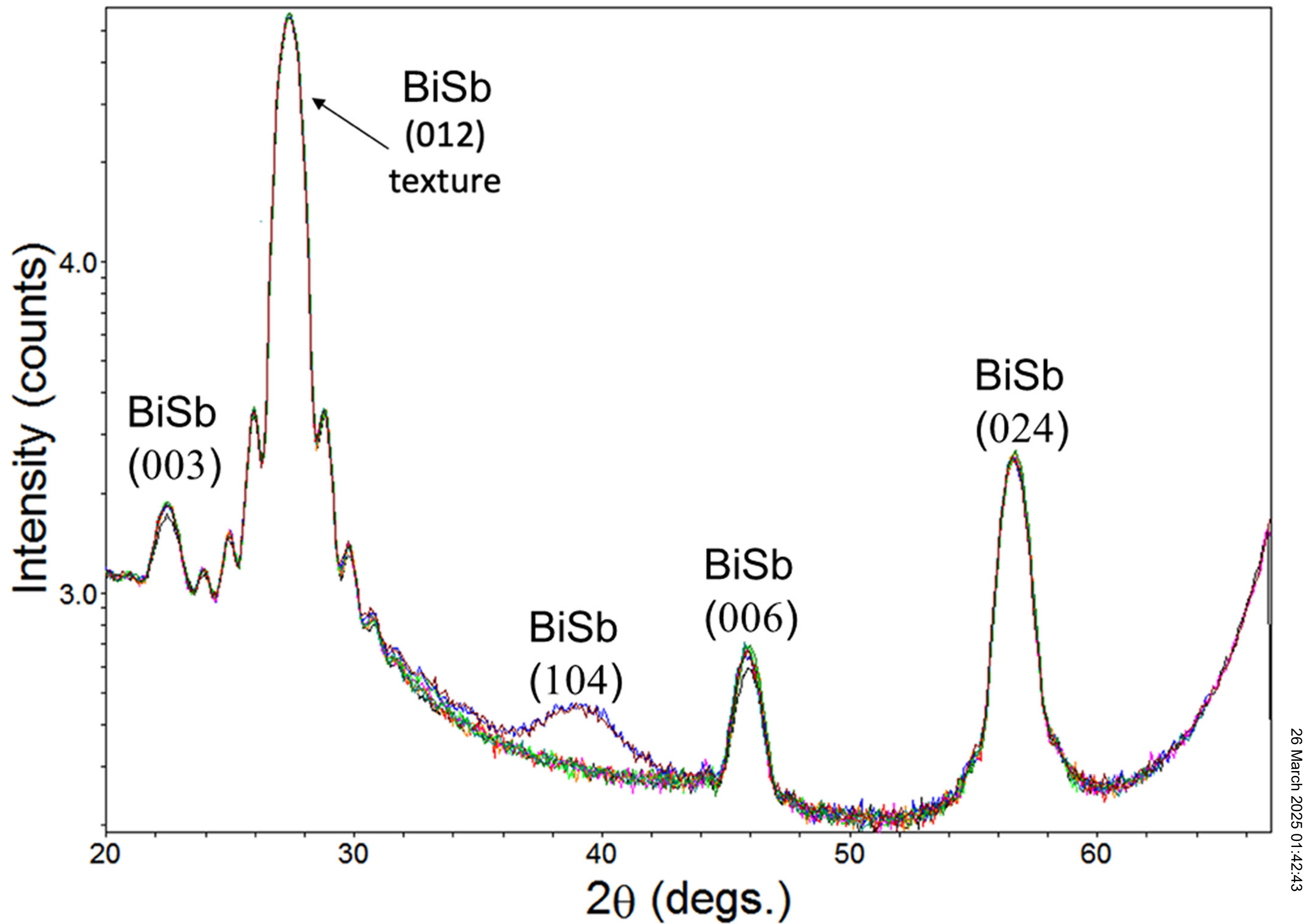

26 March 2025 01:42:43

FIG. 5. XRD results for the studied samples. The seed/buffer layers beneath the BiSb enhance the (012) orientation of the interlayer matrixed BiSb samples. Details of the seed/buffer layers can be found in Ref. 30. All the curves show the same shape, with the main BiSb(012) texture and a small BiSb(003) phase, except for two samples with an extra BiSb(104) phase. The fringes around the (012) peak indicate the smooth BiSb surface.

For the case of sample A_1 with a single NiFeGe (12 Å) ITL, the NiFeGe on the TI/ITL side helps to prevent Sb diffusion from BiSb and the migration of the FM material, which helps maintain a better spin-momentum-locked surface state and increase the intrinsic θ_{SH}, similar to the case of MgO. Furthermore, since NiFeGe is metallic, its τ_t is shorter than that of MgO. However, NiFeGe also decreases the spin-mix conductance at the ITL/FM interface, thus its τ_{mix} is longer than that of MgO. As a result, ξ^j_{DL} of NiFeGe is identical to that of MgO.

Next, we discuss sample B with the intriguing hybrid NiFeGe (9 Å)/MgO (3 Å) ITL, which yields the highest ξ^j_{DL}. This can be explained by considering the fact that this hybrid ITL combines both the advantage of the shorter τ_t of NiFeGe and the shorter τ_{mix} of MgO. Thus, the optimum ξ^j_{DL} of this hybrid NiFeGe (9 Å)/ MgO (3 Å) ITL compared with that of NiFeGe or MgO alone can be explained by the extrinsic effect. Moreover, in samples C_1–C_3, a consistent reduction in ξ^j_{DL} is observed with increasing TiO concentration into MgO to form MgTiO while maintaining the same physical thickness. Although both TiO and MgO are insulators, the bandgap of TiO is larger than that of MgO. Therefore, with the increase in the TiO concentration, τ_t increases, reducing ξ^j_{DL}, accordingly to the extrinsic mechanism. Our results have demonstrated that the ITL can have both intrinsic and extrinsic benefits on ξ^j_{DL}.

V. ESTIMATED POWER CONSUMPTION OF THE VARIOUS INTERLAYER

From the perspective of device applications, power consumption is a critical factor for SOT-MRAM and direct spin Hall effect-based magnetic sensors. The energy efficiency is influenced by ξ^j_{DL} and the conductivity of the SOT layer. Additionally, the conductivity of the layers adjacent to the spin Hall channel plays a vital role. These

© Author(s) 2025

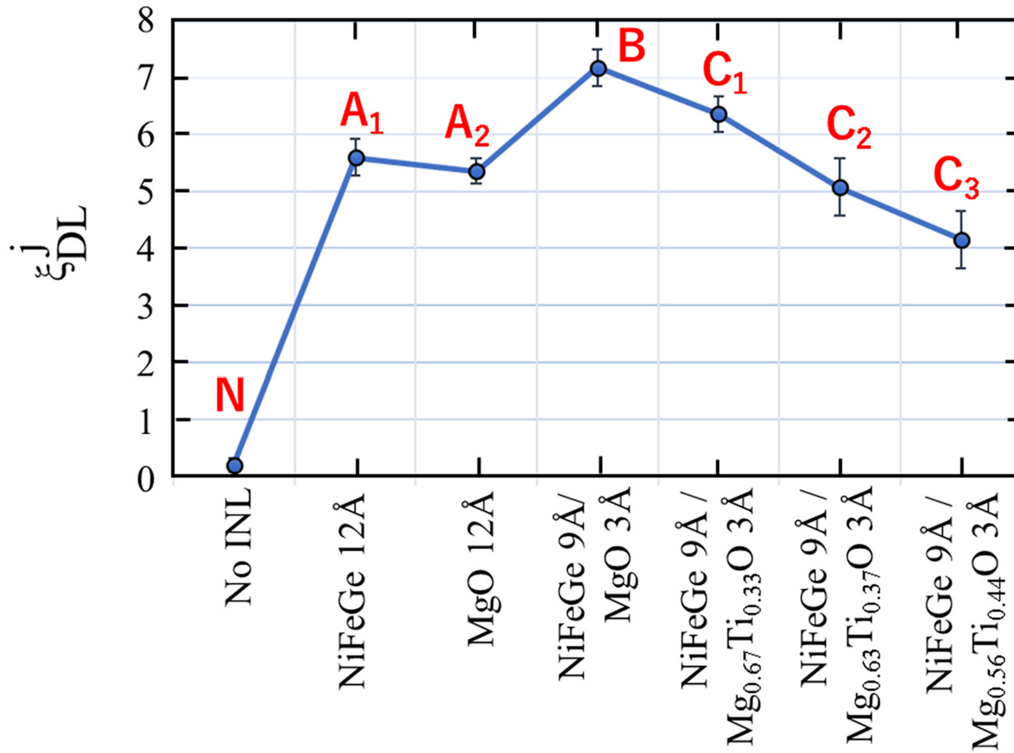

FIG. 6. ξ^{j}_{DL} as the function of metal, oxide, and hybrid metal/oxide interlayers.

26 March 2025 01:42:43

adjacent layers can partially shunt the input current flowing into the SOT layer, adding an extra component to the overall power consumption. Consequently, the SOT power consumption is expressed as

$$\text{Power} \sim \frac{1}{\xi^{j\,2}_{DL}} \frac{\sigma_{others} t_{others} + \sigma_{SOT} t_{SOT}}{(\sigma_{SOT} t_{SOT})^2},$$

where ξ^{j}_{DL}, σ_{SOT}, and t_{SOT} are the charge-to-spin conversion efficiency, electrical conductivity, and thickness of BiSb, and σ_{others} and t_{others} and are the electrical conductivity and thickness of the remaining layers including the buffer, ITL, and FM layers, which were derived from control stacks without BiSb. We normalized the power consumption by that of a reference sample with a 10 nm-thick Ta layer, which shows $\xi^{j}_{DL} = 0.18$.

Figure 7 shows the estimated normalized power consumption of those BiSb stacks by varying metal, oxide, and hybrid metal/oxide interlayers relative to the conventional Ta-based SOT (assumed to be 100%). It is clear that all BiSb stacks, no matter what ITL layers have been used, showed about up to two orders of power reduction compared to Ta. This effect is mainly driven by the higher effective spin Hall angle for BiSb.

Within the various interlayer groups, power reduction by about a factor of 2 is seen for the NiFeGe/MgO interlayer, indicating less current shunting effect. With the introduction of TiO into MgO, we

TABLE I. Summary of ILT, their intrinsic effect on θ_{SH}, their extrinsic effect on T_{IST} via τ_t and τ_{mix}, and the resulting effect on ξ^{j}_{DL}.

Sample	ITL layer	θ_{SH} (intrinsic)	T_{IST} (extrinsic)	ξ^{j}_{DL}
N	No ITL	Low	$\sim\tau_{mix}^{-1}$ with very long τ_{mix}	Low
A_1	NiFeGe 12 Å	High	$\sim(\tau_t + \tau_{mix})^{-1}$ with short τ_t, long τ_{mix}	High
A_2	MgO 12 Å	High	$\sim(\tau_t + \tau_{mix})^{-1}$ with long τ_t, short τ_{mix}	High
B	NiFeGe 9 Å/MgO 3 Å	High	$\sim(\tau_t + \tau_{mix})^{-1}$ with short τ_t, short τ_{mix}	Highest
C_1 C_2 C_3	NiFeGe 9 Å/$Mg_{1-x}Ti_xO$ 3 Å ($x = 0.33$, 0.37,0.44)	High	$\sim(\tau_t + \tau_{mix})^{-1}$ with short τ_t but increasing with x, short τ_{mix}	High but decreasing with x

© Author(s) 2025

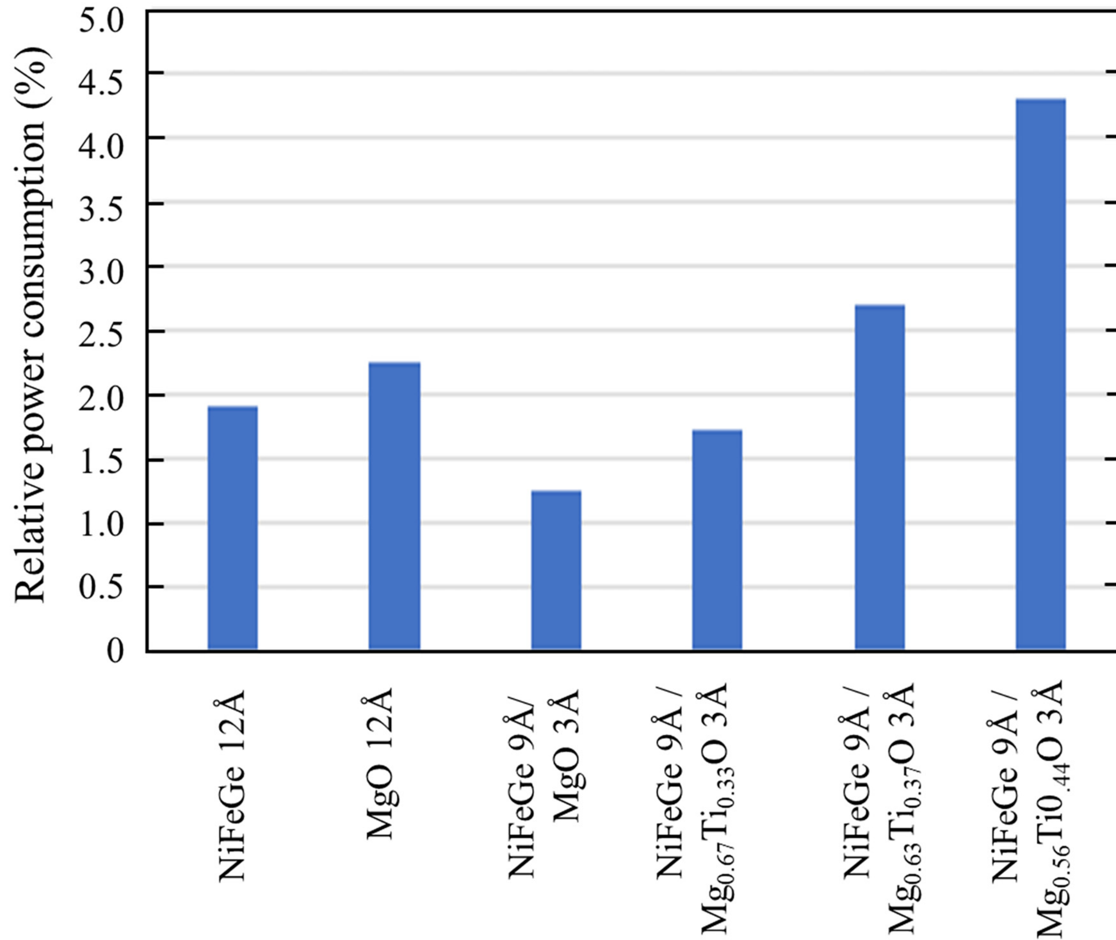

FIG. 7. Power consumption as the function of interlayers, relative to that of Ta.

26 March 2025 01:42:43

observe a slightly upward power consumption trend with increasing TiO concentration inside MgTiO. On the other hand, the resistivity of the full stacks with different MgTiO does not change significantly, implying an essentially constant charge current inside the BiSb. Thus, such increased power consumption reflects the less efficient spin current injection (smaller ξ_{DL}^{j}) into FMs with increasing TiO composition in MgTiO, as seen in Fig. 6.

VI. SUMMARY

We thoroughly studied the impact of different metal, oxide, and hybrid metal/oxide interlayers on the charge-to-spin conversion efficiency of BiSb thin films. Our findings revealed that utilizing a NiFeGe or MgO interlayer resulted in nearly the same high efficiency, with the highest efficiency achieved when using hybrid NiFeGe/MgO interlayers. However, efficiency decreased when NiFeGe was combined with MgTiO with increasing TiO composition. Such behaviors can be qualitatively understood by considering the ITL intrinsic effect of enhancing the intrinsic θ_{SH} via preventing Sb diffusion from BiSb and migration of the FM, and the extrinsic effect where the ITL spin transparency is determined by τ_t and τ_{mix}. Our results establish a framework for understanding ultrahigh θ_{SH} and provide guidance for optimizing the interlayer material and providing an effective energy-efficient solution for SOT device technologies.

AUTHOR DECLARATIONS

Conflict of Interest

Q.L., X.L., L.X., S.L., M.M., T.F., Y.T., and H.T. are in charge of research and development of new technologies at Western Digital Inc. The wafers used in this work were manufactured at Western Digital Inc. facility.

Author Contributions

Quang Le: Conceptualization (equal); Formal analysis (lead); Funding acquisition (lead); Supervision (equal); Validation (equal); Visualization (lead); Writing – original draft (lead). **Xiaoyong Liu:**

© Author(s) 2025

Data curation (equal); Formal analysis (equal); Investigation (equal); Methodology (equal); Validation (equal). **Lei Xu:** Investigation (equal); Methodology (equal); Resources (equal); Visualization (equal). **Brian R. York:** Conceptualization (equal); Data curation (equal); Formal analysis (equal); Investigation (equal); Methodology (equal); Resources (equal); Visualization (equal). **Cherngye Hwang:** Conceptualization (equal); Investigation (equal); Methodology (equal); Resources (equal). **Son Le:** Data curation (equal); Investigation (equal); Methodology (equal); Resources (equal). **Maki Maeda:** Project administration (lead); Resources (equal). **Tuo Fan:** Data curation (equal); Formal analysis (equal); Investigation (equal); Methodology (equal). **Yu Tao:** Data curation (supporting); Formal analysis (supporting); Investigation (supporting); Methodology (supporting). **Hisashi Takano:** Funding acquisition (lead); Supervision (lead). **Min Liu:** Investigation (supporting); Methodology (supporting). **Zhang Ruixian:** Investigation (supporting); Methodology (supporting). **Shota Namba:** Investigation (supporting); Methodology (supporting). **Pham Nam Hai:** Conceptualization (equal); Formal analysis (equal); Funding acquisition (lead); Resources (equal); Supervision (lead); Validation (equal); Visualization (supporting); Writing – review & editing (equal).

DATA AVAILABILITY

The data that support the findings of this study are available from the corresponding authors upon reasonable request.

REFERENCES

[1]S. Murakami, N. Nagaosa, and S.-C. Zhang, Science **301**, 1348 (2003).
[2]L. Liu, T. Moriyama, D. C. Ralph, and R. A. Buhrman, Phys. Rev. Lett. **106**, 036601 (2011).
[3]C.-F. Pai *et al.*, Appl. Phys. Lett. **101**, 122404 (2012).
[4]L. Liu, C.-F. Pai, Y. Li, H. W. Tseng, D. C. Ralph, and R. A. Buhrman, Science **336**, 555 (2012).
[5]A. R. Mellnik *et al.*, Nature **511**, 449 (2014).
[6]H. Wu, P. Zhang, P. Deng, Q. Lan, Q. Pan, S. A. Razavi, X. Che, L. Huang, B. Dai, K. Wong, X. Han, and K. L. Wang, Phys. Rev. Lett. **123**, 207205 (2019).
[7]N. H. D. Khang, Y. Ueda, and P. N. Hai, Nat. Mater. **17**, 808 (2018).
[8]T. Shirokura, T. Fan, N. H. D. Khang, T. Kondo, and P. N. Hai, Sci. Rep. **12**, 2426 (2022).
[9]T. Shirokura and P. N. Hai, AIP Adv. **12**, 125116 (2022).
[10]S. Kagami, T. Shirokura, and P. N. Hai, Jpn. J. Appl. Phys. **63**, 02SP98 (2024).
[11]Y. Ueda, N. H. D. Khang, K. Yao, and P. N. Hai, Appl. Phys. Lett. **110**, 062401 (2017).
[12]T. Fan, M. Tobah, T. Shirokura, N. H. D. Khang, and P. N. Hai, Jpn. J. Appl. Phys. **59**, 063001 (2020).
[13]T. Fan, N. H. D. Khang, S. Nakano, and P. N. Hai, Sci. Rep. **12**, 2998 (2022).
[14]J. Sasaki, H. H. Huy, N. H. D. Khang, P. N. Hai, Q. Le, B. York, X. Liu, S. Le, C. Hwang, M. Ho, and H. Takano, IEEE Trans. Magn. **58**, 3200404 (2022).
[15]J. Sasaki, S. Namba, S. Takahashi, Y. Hirayama, and P. N. Hai, Jpn. J. Appl. Phys. **62**, SC1005 (2023).
[16]H. Y. Poh, C. C. I. Ang, G. J. Lim, T. L. Jin, S. H. Lee, E. K. Koh, F. Poh, and W. S. Lew, Phys. Rev. Appl. **19**, 034012 (2023).
[17]H. H. Huy, Z. Ruixian, T. Shirokura, S. Takahashi, Y. Hirayama, and P. N. Hai, IEEE Trans. Magn. **59**, 3400905 (2023).
[18]T. Manolj, Z. Wen, J. Uzuhashi, T. Ohkubo, H. Sukegawa, C. Murapaka, B. York, X. Liu, Q. Le, and S. Mitani, ACS Appl. Electron. Mater. **6**, 4269 (2024).
[19]L. Zhu, D. C. Ralph, and R. A. Buhrman, Phys. Rev. B **99**, 180404(R) (2019).
[20]M. Hayashi, J. Kim, M. Yamanouchi, and H. Ohno, Phys. Rev. B **89**, 144425 (2014).
[21]N. H. D. Khang and P. N. Hai, Appl. Phys. Lett. **117**, 252402 (2020).
[22]S. Zhang and A. Fert, Phys. Rev. B **94**, 184423 (2016).
[23]H. Isshiki, P. Muduli, J. Kim, K. Kondou, and Y. Otani, Phys. Rev. B **102**, 184411 (2020).
[24]H. He, L. Tai, H. Wu, D. Wu, A. Razavi, T. A. Gosavi, E. S. Walker, K. Oguz, C.-C. Lin, K. Wong *et al.*, Phys. Rev. B **104**, L220407 (2021).
[25]W. Chen, J. Phys.: Condens. Matter **32**, 035809 (2020).
[26]S. Ghosh and A. Manchon, Phys. Rev. B **97**, 134402 (2018).
[27]W. Chen, Phys. Rev. B **102**, 144442 (2020).
[28]A. Natarajarathinam, Z. R. Tadisina, T. Mewes, S. Watts, E. Chen, and S. Gupta, J. Appl. Phys. **112**, 053909 (2012).
[29]S. Kim, S. C. Baek, M. Ishibashi, K. Yamada, T. Taniguchi, T. Okuno, Y. Kotani, T. Nakamura, K.-J. Kim, T. Moriyama *et al.*, Appl. Phys. Express **10**, 073006 (2017).
[30]Q. Le, C. Hwang, B. R. York, T. A. Nguyen, Z. Gao, K. San Ho, and P. N. Hai, U.S. patent 11,694,713 (4 July 2023).

26 March 2025 01:42:43

© Author(s) 2025